Acta Materialia 124 (2017) 608–619

Contents lists available at ScienceDirect

Acta Materialia

journal homepage: www.elsevier.com/locate/actamat

Full length article

Directional solidification of aqueous TiO_2 suspensions under reduced gravity

Kristen L. Scotti [a], Emily E. Northard [a], Amelia Plunk [a], Bryce C. Tappan [b], David C. Dunand [a, *]

[a] Department of Materials Science and Engineering, Northwestern University, Evanston, IL 60208, USA
[b] Los Alamos National Laboratory, Los Alamos, NM 87545, USA

ARTICLE INFO

Article history:
Received 4 August 2016
Received in revised form
12 November 2016
Accepted 14 November 2016
Available online 1 December 2016

Keywords:
Microgravity
Freeze casting
Parabolic flights
Ice banding
Ice-templating

ABSTRACT

Porous materials exhibiting aligned, elongated pore structures can be created by directional solidification of aqueous suspensions—where particles are rejected from a propagating ice front and form interdendritic, particle-packed walls—followed by sublimation of the ice, and sintering of the particle walls. Theoretical models that predict dendritic lamellae spacing—and thus wall and pore width in the final materials—are currently limited due to an inability to account for gravity-driven convective effects during solidification. Here, aqueous suspensions of 10–30 nm TiO_2 nanoparticles are solidified on parabolic flights under micro-, lunar (~0.17 g; $g_l = 1.62$ m/s^2), and Martian (~0.38 g; $g_m = 3.71$ m/s^2) gravity and compared to terrestrially-solidified samples. After ice sublimation and sintering, all resulting TiO_2 materials exhibit elongated lamellar pores replicating the ice dendrites. Increasing the TiO_2 fraction in the suspensions leads to decreased lamellar spacing in all samples, regardless of gravitational acceleration. Consistent with previous studies of microgravity solidification of binary metallic alloys, lamellar spacing decreases with increasing gravitational acceleration. Mean lamellar spacing for 20 wt% TiO_2 nanoparticles suspensions under micro-, lunar, Martian, and terrestrial gravity are, respectively: 50 ± 8, 34 ± 11, 30 ± 6, and 23 ± 9 μm, indicating that gravity-driven convection strongly affects lamellae spacing under terrestrial gravity conditions. Gravitational effects on lamellar spacing are highest at low TiO_2 fractions in the suspension; for 5 wt% TiO_2 suspensions, the microgravity lamellar spacing is more than twice that under terrestrial gravity (182 ± 21 vs. 81 ± 23 μm). Results of this study are in good agreement with previous studies of binary metallic alloy solidification where primary dendrite spacing increases under microgravity. Literature data from ice-templating systems are used to discuss a dependence on lamellae spacing of the density ratio of particles and fluid.

1. Introduction

Directional solidification of aqueous suspensions is an ice-templating technique that is used to create materials with highly anisotropic pore structures [1–7]. In a first step, an aqueous suspension of particles is solidified under the presence of a thermal gradient. Colonies of lamellar ice dendrites (hereafter, "lamellae"), oriented perpendicular to the freezing substrate and parallel to each other, propagate along the direction imposed by the temperature gradient, while rejecting particles away from the moving front. Rejected particles form an accumulation layer directly ahead of the solidification interface. As solidification progresses, lamellae break through the accumulation region, and particles are concentrated within the interdendritic spaces [8]. After solidification, ice is removed via sublimation, leaving lamellar macropores (which template the ice lamellae) surrounded by particle-packed walls. These walls are self-supporting when binder dissolved in the liquid is rejected together with the particles. Lastly, the resulting porous structure is heat-treated to sinter and densify the particle-packed walls. The ice-templating technique has gained considerable attention because it allows for the tailoring of pore width, length, orientation, volume fraction, and connectivity, and it has been utilized as a processing route for porous ceramic [9], polymeric [10], metallic [11], pharmaceutical [12,13], foodstuff [14,15], and biological [2,16] materials.

The microstructural characteristics of ice-templated materials

* Corresponding author.
E-mail address: dunand@northwestern.edu (D.C. Dunand).

http://dx.doi.org/10.1016/j.actamat.2016.11.038
1359-6454/

are largely determined by the solidification behavior of the water and the rejection of the particles by the growing solid lamellae. Whereas various parameters, *e.g.*, cooling rates [17], solidification velocity [18], particle fraction within the suspension [19], suspension additives [20,21] and stability [22], and sample height [23], have been explored previously, little is known about the effect of gravity-driven convection on the solidified microstructural formation.

In binary systems, where solute is rejected by the interface, a solute-rich region accumulates ahead of the solidification front, similar to the particle-rich region that develops during ice-templating as a result of particle rejection at the interface. This solute-enriched region becomes constitutionally undercooled (*i.e.*, the freezing temperature is locally depressed with respect to the bulk system) for systems in which the liquidus temperature is inversely related to the concentration of solute (or particles) in the fluid [24]. A mushy layer, which is a two-phase boundary region that consists of solute-free dendrites within a solute-rich fluid, forms below the particle/solute accumulation region. The mushy layer is often described as a reactive porous medium [25] because the permeability of this region is dynamically responsive to mass and heat transfer within the bulk fluid region. Gravity-induced convective fluid motion can result from temperature (thermal convection) and/or concentration (solutal convection) gradients both within, and ahead of (*i.e.*, within the bulk liquid) the mushy layer.

Convective plumes are predicted by numerical analysis [26] of directional solidification of colloids and are supported by experimental observation of steady-state velocity fluctuations [27] as well as Benard-Rayleigh convective cells [28]. However, due largely to the complexity of the ice-templating system and the lack of experimental data obtained in the absence of gravity-driven convection, theoretical models describing the solidification process are based on diffusive growth conditions [24,29,30] and gravity-driven convective effects are ignored. Better predictive modeling is necessary for understanding how to control microstructures templated during the solidification process. Benchmark data, unencumbered by convection, are the first step.

Here, we explore the effect of gravity-driven convection on microstructure formation by carrying out the solidification step of the ice-templating process under micro- and reduced gravity conditions on parabolic flights as well as under normal terrestrial conditions. Titanium oxide and water are utilized as the particle and fluid, respectively. Microstructural investigation of sintered structures reveals the dependence of the ice lamellae spacing (λ_L) in suspensions solidified under various gravity accelerations and for various solid fractions. These results are compared to primary dendrite spacing (λ_1) reported in the literature for binary metallic alloys solidified under reduced gravity conditions. Finally, literature data are utilized to investigate the dependence of particle-to-fluid density on λ_L in ice-templated materials.

2. Materials and methods

2.1. Colloid preparation

Colloidal suspensions of titanium dioxide nanoparticles in deionized water were prepared using a mixture of ethylene glycol (Consolidated Chemical & Solvents, LLC., Quakertown, PA) and ammonium hydroxide (SEOH, Navasota, TX) as dispersants, and agar (NOW Foods, Bloomingdale, IL) as a binder. Agar (0.2 wt% with respect to TiO_2) was added to deionized water which was boiled to dissolve the agar and degas the solution. Ethylene glycol (5 vol%, with respect to total suspension volume) and varying weight fractions (5, 8, 15, and 20 wt%, corresponding to volume fractions of 1.5, 2.5, 5, and 7%) of titanium oxide nanoparticles (TiO_2, anatase phase, 99.5% purity, 10–30 nm, specific surface area 50 $m^2\ g^{-1}$, SkySpring Nanomaterials, Inc., Houston, TX) were added to the aqueous solution. Departures from the specified portions resulted in unstable suspensions. Nanometric TiO_2 was utilized here so as to reduce gravitational sedimentation to negligible levels during terrestrial experiments, since the objective of this work was to investigate gravity-driven convection. Ammonium hydroxide was subsequently added drop-wise to obtain a suspension pH of 10 and stirred for 30 min using a magnetic stirrer. The colloidal suspensions were injected into molds made from tin-plated steel (79 × 35 × 3 mm) for 5 and 8 wt% TiO_2 and PVC tubing (20 mm inner diameter; 3 mm height) for 15 and 20 wt% TiO_2; a syringe was used to prevent transfer of air bubbles. Molds were sealed on both ends to ensure no air pockets between fluid and seal were present. One end of each mold was sealed with thermally-conductive copper foil to improve heat conduction and promote unidirectional freezing; the other side was sealed with insulating styrene-butadiene rubber plugs.

2.2. Parabolic flight testing

Directional solidification experiments were performed over the course of two NASA Flight Opportunities Program flight campaigns during 2014 and 2015. Each campaign consisted of four flights in the NASA C-9 aircraft [31]. A microgravity environment was obtained through a series of parabolic maneuvers (~50 per flight) which result in ~25 s periods of microgravity (g_μ ~ 0.00 ± 0.02 g). The microgravity parabolas were interspersed with hypergravity (~1.8 g; g_h ~ 17.6 m/s^2) period of ~90 s duration. Solidification experiments were also performed during two lunar (~0.17 g; $g_l = 1.62\ m/s^2$) and one Martian (~0.38 g; $g_m = 3.71\ m/s^2$) parabola.

2.3. Directional ice-templating

A copper box cooled to ~228 K was utilized as a freezing substrate. To ensure relatively constant temperature throughout the flight experiments, the copper box was filled with ~1 kg of dry ice (solid CO_2 sublimating at 195 K) and insulated on its sides with PVC foam. The temperature of the top surface of the box, used as the freezing substrate, was monitored and recorded throughout flight testing using a K-type thermocouple. Immediately prior to the onset of reduced gravity periods, one mold containing TiO_2 colloidal suspension was removed from a storage cooler (maintained between 276 and 281 K) and shaken for 20 s. At the onset of the reduced gravitational period, the mold was placed onto the freezing substrate, maintaining contact using manual mechanical pressure. To minimize the effect of transient gravitational accelerations, samples were removed from the freezing substrate 2–3 s prior to the termination of reduced gravitational periods, as confirmed by NASA's onboard tri-axial accelerometer display located within the research area. Each sample was solidified at an average velocity of ~100 μm/s, resulting in solidification depths of ~2.5 mm during each reduced gravity period. The solidified samples were stored on dry ice for the remainder of flight and prior to sublimation for times ranging from 30 to 200 days. Control, "terrestrial" samples were solidified for all TiO_2 solid fractions utilizing the same freezing apparatus under terrestrial gravity (1 g; $g = 9.8\ m/s^2$) conditions and subsequently stored at the same temperature and storage time as above.

2.4. Sublimation, sintering and microstructure characterization

Samples were sublimated in a freeze-dryer (Labcono, Freeze Dry System, Model 7754000) for at least 24 h at 233 K and low residual

pressure (<3 Pa). After sublimation, samples were sintered in air in a box furnace at 1173 K for 1 h, using a heating and cooling rate of 5 K/min.

Ceramographic examination was conducted using optical microscopy on mounted, ground and polished samples. X-ray diffraction (XRD, using a Rigaku DMAX diffractometer, operated at 20 mA and 40 kV) patterns were collected in the 2θ range 20–70° to identify the crystallographic phases of as-received powders and ground sintered samples. Image analysis was performed using ImageJ/Fiji. The segmentation of pore walls was obtained by applying the Otsu threshold algorithm [32] on contrast-normalized images [33]. Lamellae spacing (λ_L) was defined as described by Deville et al. [34], as the width of one wall plus its adjacent macropore, and measured using the line intercept method [35] on binary images.

3. Results

3.1. Colloid stability

Based on zeta potential values, the isoelectric point (IEP) of aqueous TiO_2 nanoparticle suspensions is between 4.5 and 6.0 [36]. For a stable suspension, the colloid must exhibit a zeta potential variation of approximately ±40 eV from the IEP; therefore, TiO_2 colloidal suspensions can be stabilized in two pH ranges: 2.5–3.5 *or* 9.5–10.5. Initial tests performed with HCl and NH_3 showed that stabilization was easier to achieve in the basic range. Subsequent sedimentation tests were conducted on 8 and 20 wt% TiO_2 colloidal suspensions in the basic range, using NH_3 to obtain pH of 9.5, 10, or 10.5. Colloidal suspensions were monitored over the course of 3 h. Immediate settling was observed for the two suspensions with the lower pH values. However, no sedimentation layer was observed in the suspension with a pH of 10.5. Accordingly, all colloidal suspensions used for solidification experiments were prepared at pH 10.5.

3.2. Directional solidification

A total of 59 samples were analyzed: 35 reduced-gravity samples solidified on parabolic flights and 24 control ("terrestrial") samples, solidified under normal terrestrial gravity. All but three parabolic flight samples were solidified under microgravity conditions (~0 g) with solid fractions provided in Table 1; two samples (15 and 20 wt% TiO_2) were solidified under lunar gravitational conditions and one sample (20 wt% TiO_2) was solidified under Martian gravitational conditions. Colloidal suspensions of 5 and 8 wt% TiO_2 were solidified during the 2014 flight campaign using rectangular tin-plated steel molds. Although precautions were taken to minimize the transfer of air bubbles during filling, post-flight microstructural investigation indicated the probable presence of bubbles in four samples. Similar to observations by Grugel et al. [37], the presence of bubbles disrupted the dendritic array under microgravity conditions. No quantitative measurements were taken from samples disrupted by bubbles and they are not included in Table 1. PVC cylindrical molds were utilized during 2015 flights with colloids containing 15 and 20 wt% TiO_2; the presence of bubbles was not observed during microstructural analysis. Control samples were solidified under normal terrestrial gravity using the tin-plated steel molds for 5 and 8 wt% TiO_2 and the PVC molds for the 15 and 20 wt% TiO_2.

As a result of dry ice sublimation inside the copper box, the temperature of the freezing substrate increased slowly from 228 to 235 K over the course of each flight (1.5 h). Regression analysis on mean lamellae spacing λ_L for each sample studied in combination with the associated freezing substrate temperature revealed no significant correlation for any TiO_2 weight fraction under study. Similarly, analysis of accelerometer data to determine any systematic variation in residual gravitational acceleration revealed no significant correlation for any TiO_2 weight fraction.

Coarsening of ice structures can occur in ice-templated materials if the storage temperature is above the glass transition temperature. In solidified colloidal systems, the glass transition temperature is dependent on the system's ability to restrict mass transfer; specifically, the concentration and type of particle and suspension additives (*e.g.,* polymer binders) within the particle-packed walls [6]. To assess the effect of storage on coarsening in microgravity-solidified samples, terrestrial samples were examined that were stored on dry ice for 0–200 days after solidification at 228–235 K. No significant difference between the mean dendritic lamellae spacing among these samples could be detected. It is thus very likely that no appreciable coarsening of the ice dendrites occurred during storage of the reduced-gravity samples, as the storage temperature of ~195 K, was well below that of the estimated glass transition temperatures (242–272 K) for all of the aqueous colloidal systems reviewed by Pawlec et al. [6].

3.3. Crystalline structure

X-ray diffraction (XRD) patterns of as-received TiO_2 powder as well as ice-templated samples sintered for 1 h at 1173 or 1273 K and subsequently ground into powder are presented in Fig. 1. Compared with as-received powders in the anatase phase (Fig. 1(a)), the

Table 1
Summary of microstructural parameters (lamellae spacing, pore width, and wall width) based on metallographic investigation of 53 samples (N = number of samples) created from slurries with various TiO_2 volume fractions solidified under microgravity (0 m/s^2) and terrestrial (9.81 m/s^2) conditions. Parameters for samples solidified under lunar (1.62 m/s^2) and Martian (3.71 m/s^2) gravitational conditions are also provided. Lamellae spacing (λ_L) was measured using the method of Deville et al. [34].

TiO_2 (wt%)	g (m/s^2)	N	Lamellae spacing, λ_L (μm)		Pore width (μm)		Wall width (μm)		Linear shrinkage (%)
			Mean	Std. dev.	Mean	Std. dev.	Mean	Std. dev.	
5	0	8	182	21	116	24	66	30	20
	9.81	6	81	23	36	18	46	29	
8	0	8	153	16	91	20	53	26	18
	9.81	6	55	12	35	12	24	9	
15	0	8	119	17	70	25	46	14	16
	1.62	1	92	20	58	31	42	27	
	9.81	6	36	12	18	7	18	6	
20	0	8	50	8	22	10	32	8	15
	1.62	1	34	11	14	3	19	5	
	3.71	1	30	6	9	3	19	6	
	9.81	6	23	9	11	7	20	11	

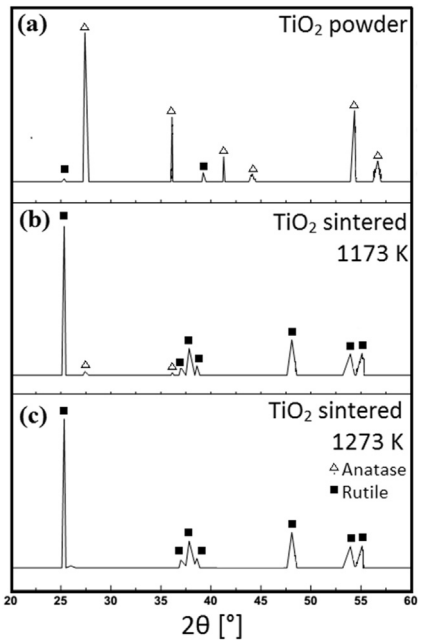

Fig. 1. X-ray diffraction (XRD) patterns of TiO_2 (a) initial powder and (b) sintered at 1173 K for 1 h and (c) 1273 K for 1 h.

sample sintered at 1173 K, with a diffraction peak at 27.4°, has partially transformed to rutile, but the predominant phase is still anatase as indicated by the predominant peak at 25.3° (Fig. 1(b)). Transformation from anatase to rutile is expected to begin around 723 K, however transformation is a time-dependent process [38]. The anatase phase was similarly retained by Ren et al., for ice-templated TiO_2 materials when sintering for 1 h at 1273 K [39]. For comparison purposes, ground ice-templated TiO_2 samples sintered at 1273 K, above the sintering temperature used for sample analysis, were also tested; XRD patterns show full transformation to rutile (Fig. 1(c)).

3.4. Solidification microstructure

3.4.1. Ice lamellae

Colloidal suspensions from all weight fractions solidified under micro-, lunar, Martian, and terrestrial gravity exhibited, elongated, directional pores, aligned in the direction of the temperature gradient (Fig. 2). After sublimation and sintering, linear shrinkage ranging from 20 to 15% was observed for 5 to 20 wt% TiO_2 samples, respectively, irrespective of gravity condition (Table 1). The microstructure of the ice-templated samples is described by the average lamellae spacing (λ_L) taken perpendicular to the freezing direction. This is equivalent to the center-to-center inter-lamellae spacing, but is measured as the sum of the widths of a ceramic wall and its adjacent macropore [34]. Fig. 3(a) shows the mean value of λ_L as measured for sintered samples solidified under micro-, lunar, and terrestrial gravitational conditions plotted against the solid loading fraction. All microstructural experimental data are provided in Table 1; in total, 664 measurements of λ_L were taken, ensuring no measurements were repeated on the same pore structures. Increasing the solid fraction in the colloid leads to decreased λ_L in both microgravity and terrestrial samples. For all weight fractions studied, λ_L is highest under microgravity conditions and decreases with increasing gravitational acceleration. Fig. 3(b) and (c) show pore and wall width, respectively, plotted against TiO_2 weight fraction. As can be expected based on λ_L, pore and wall width increase in microgravity samples of similar solid loadings as compared to terrestrial samples, at all particle weight fractions.

As the solid loading increases to 20 wt% TiO_2, a sharp decline in the ratio between λ_L obtained under micro- and terrestrial gravity is observed. Specifically, at 15 wt% TiO_2, λ_L increases under microgravity conditions by about a factor of 3; at 20 wt% TiO_2, it increases only by a factor of 2. Fig. 4(a–c) shows the mean values of lamellae spacing (λ_L), pore width, and wall width, respectively, for sintered samples with TiO_2 loadings of 20 wt% under all gravitational conditions. Mean pore width as measured here for 20 wt% TiO_2 under normal terrestrial gravity (11 μm) is in relative agreement with that measured by Ren et al. [40], for 20 wt% TiO_2 solidified using a substrate temperature of 255 K (13.6 μm). Decreased pore size observed here can be explained by the lower substrate temperature employed (~232 K). A clear dependence of λ_L and pore width on gravitational acceleration is observed. Wall width is similarly increased under microgravity conditions relative to terrestrial, but remains relatively constant for samples solidified under lunar, Martian, and terrestrial conditions.

3.4.2. Ice lenses

Periodic ice lenses (*i.e.*, ice banding) were observed in two of the eight 20 wt% TiO_2 colloids solidified under terrestrial gravitational conditions. These periodic structures consisted of numerous parallel ice lenses, which are planar regions of pure ice, interspersed

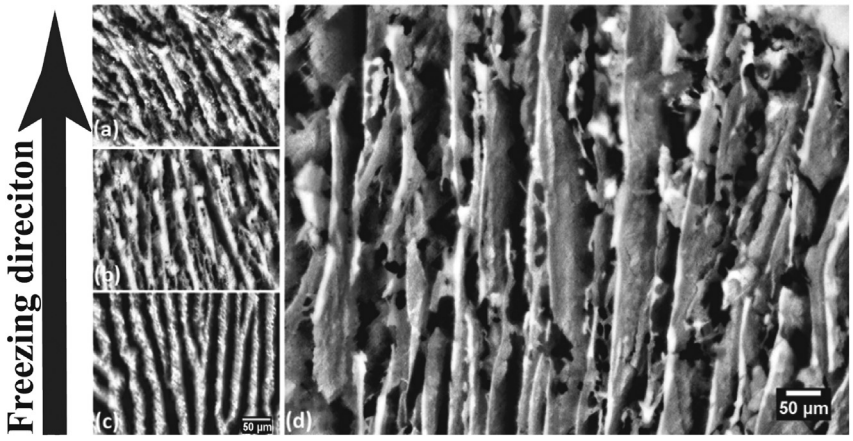

Fig. 2. Longitudinal cross-sections of sintered TiO_2 samples sintered from 20 wt% TiO_2 aqueous suspensions directionally solidified under (a) terrestrial, (b) Martian, (c) lunar, and (d) microgravity conditions. The 10 μm scale bar in (c) applies to the three micrographs (a–c).

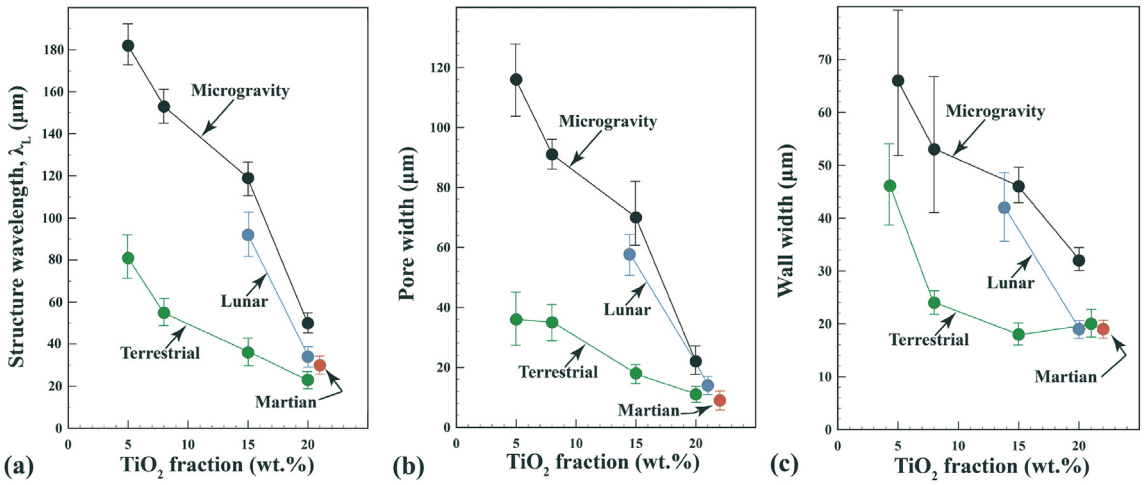

Fig. 3. Plot of (a) lamellae spacing (λ_L), (b) pore width, and (c) wall width in sintered samples as a function of TiO_2 solid fraction for slurries solidified under reduced and terrestrial gravitational conditions.

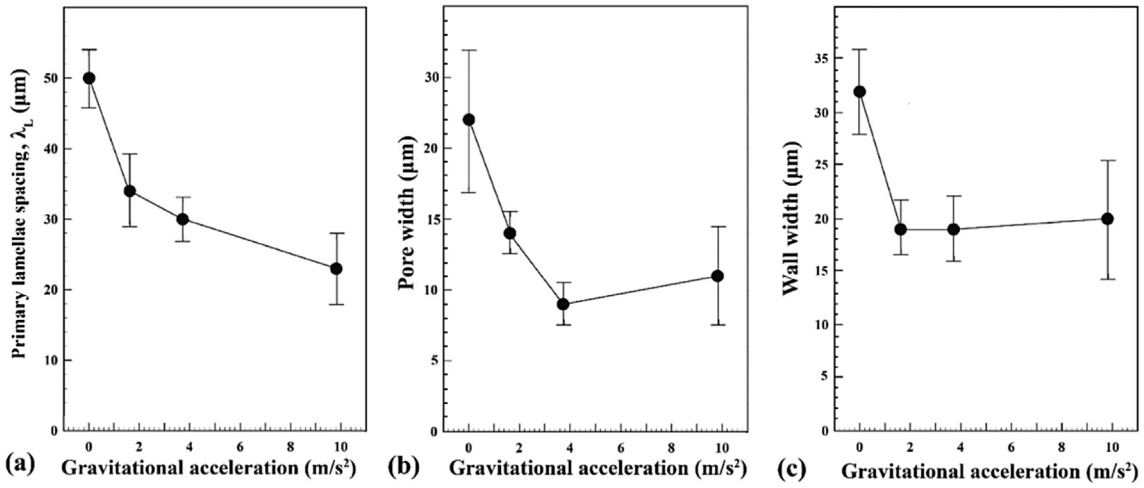

Fig. 4. Plot of (a) lamellae spacing (λ_L), (b) pore width, and (c) wall width in sintered samples created from 20 wt% TiO_2 slurries vs. gravitational acceleration.

between particle-packed beds oriented parallel to the solidification direction (unlike lamellae, which are oriented perpendicular to the freezing direction) [41–48]. Periodic ice lenses are shown in Fig. 5 for one of the two 20 wt% TiO_2 terrestrial samples, with red arrows indicating individual ice lenses. For both samples, periodic ice lenses extended the full height of the sample (with respect to the freezing direction) and measured 1.5 and 2 mm across the main diameter of 20 mm in each respective sample. Quantitative measurements were not taken from these samples and they are not included in the sample count (N) listed in Table 1. Small regions of periodic ice lenses (extending 50–300 μm longitudinally and 200–350 μm transversely to the freezing direction, respectively) were also observed in three of the remaining six 20 wt% TiO_2 colloids solidified under terrestrial gravity. Ice lenses were not observed in any of the 32 samples solidified under reduced gravity or for any of the lower solid loadings, independent of gravity values.

4. Discussion

4.1. Primary spacing

4.1.1. Lamellae spacing λ_L

The dependence of lamellae spacing (λ_L) on gravitational acceleration depicted in Figs. 3(a) and 4(a), demonstrates that, in the case of the TiO_2 colloids solidified here, gravity-driven convection reduces λ_L. In the ice-templating literature [34,49,50], an empirical power-law dependence of lamellae spacing (λ_L, sometimes called structure wavelength) on interface velocity (v) is well demonstrated under terrestrial conditions:

$$\lambda_L \propto v^n, \tag{1}$$

where n typically varies between −0.2 and −1.3 [18,34,49]. Increasing v leads to faster ice growth and results in thinner lamellae and lower values of λ_L [5].

The relationship between v and λ_L is more complex than that portrayed by Eq. (1). It is expected that any suspension characteristic or solidification conditions that alters particle-fluid, particle-solid, or particle-particle behavior, can affect λ_L, including, but not limited to: particle size and volume fraction; temperature gradient and cooling rate. Additional complexity arises from the interdependent nature of many of these parameters; synergistic and antagonistic effects are probable, but poorly understood. For example, Deville et al., found decreasing the size of Al_2O_3 particles from 400 to 100 nm resulted in a change in exponent n from −1 to −0.67; that is, decreasing particle size was found to result in a

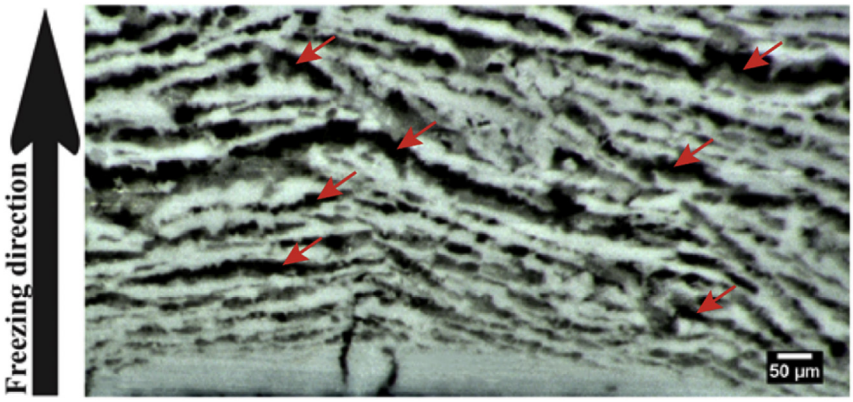

Fig. 5. Longitudinal cross-sections of a sintered TiO_2 sample sintered from a 20 wt% TiO_2 aqueous suspension directionally solidified under terrestrial conditions, showing periodic ice lenses perpendicular to the freezing direction. White areas represent sintered TiO_2 particle walls and dark areas represent pores, templated by individual ice lenses (red arrows). The ~70 μm thick white band at the bottom of the image is the bottom of the sample, consisting of densely sintered TiO_2, which was in contact with the freezing substrate. (For interpretation of the references to colour in this figure legend, the reader is referred to the web version of this article.)

reduction of λ_L [34]. Comparatively, Miller et al., calculated an exponent value of $n = -0.69$ for 350 nm Al_2O_3 [49]. In our water-TiO_2 system solidified rapidly (~100 μm/s), λ_L shows dependence on particle fraction, as pointed out previously for Al_2O_3 suspended in camphene, solidified at much slower velocities (ranging from 0.1 to 0.6 μm/s) [8].

4.1.2. Primary dendrite spacing (λ_1) in binary metallic alloys

Ice-templating has been compared to solidification of binary metallic alloy systems [49,51,52], where particles (TiO_2, in our case) take on the role of the solute and the fluid (here, water) is the solvent. Lamellae spacing, λ_L in ice-templated materials, then corresponds to primary dendrite spacing (λ_1) in metal alloy systems. The schematic in Fig. 6, illustrates how λ_1 and λ_L are measured. In ice-templated materials, λ_L is the distance comprising one macropore plus its adjacent wall, whereas, in metal alloys, λ_1 is measured by taking the distance between dendrite centers.

Numerous models have been developed for predicting λ_1 in metallic alloys [53–55]. However, most of the studies included in the forthcoming analysis utilize the Hunt and Lu [56] model for purposes of theoretical comparison. Using this model, a simplified relation for λ_1 can be described as a function of solidification velocity (v) and imposed temperature gradient (G):

$$\lambda_1 \propto v^{-1/4} G^{-1/2} \tag{2}$$

Similarly to Eq. (1), the above equation predicts a decrease in λ_1 with increasing solidification velocity, but also takes into account the imposed temperature gradient, which is likewise, inversely related to λ_1. This model is valid only under diffusive conditions or for systems in which λ_1 is not influenced strongly by gravity-driven convective effects.

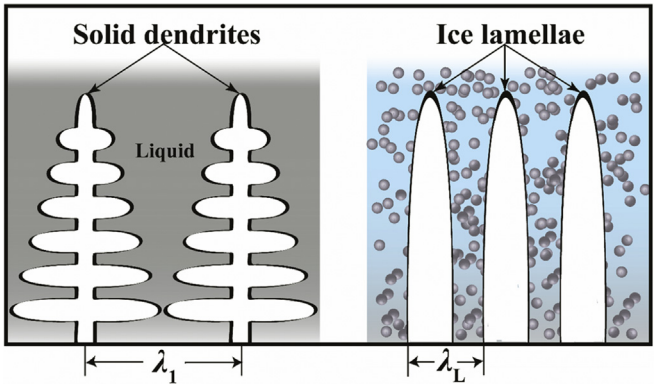

Fig. 6. Comparison between (a) primary dendrite spacing (λ_1) as measured in alloys and (b) lamellae spacing (λ_L) as measured in ice-templated materials.

4.2. Gravity-driven convective regimes

Convective regimes during directional solidification can generally be categorized by considering: (i) the direction of solidification with respect to the gravity vector, and (ii) the relative density of the rejected solute to solvent ($\rho_{solute}/\rho_{solvent}$). Here, we focus on solidification advancing vertically upwards (liquid above and solid below), against the gravitational field, as this orientation stabilizes thermal and solutal convection resulting from axial gradients [57].

In classical "thermosolutal convection" (or double-diffusive convection), solute of lesser density than the solvent is rejected at the interface ($\rho_{solute}/\rho_{solvent} < 1$; *e.g.,* hypoeutectic Pb-Sn alloys). In this case, buoyancy-driven convective flow results from the combination of thermal and concentration gradients. Conversely, when solute of greater relative density is rejected at the interface ($\rho_{solute}/\rho_{solvent} > 1$; *e.g.,* hypoeutectic Al-Cu alloys; ice-templating), density stratifications (whether due to axial thermal and/or concentration gradients) are stabilized against buoyancy-driven fluid motion [58]. However, convective fluid motion is still possible in the presence of lateral temperature and/or concentration gradients. These are known to occur when (a) the thermal conductivity of the mold is higher than the solidified solvent [59] and/or (b) there is a thermal conductivity mismatch between the liquid and solid phases [60]. In these cases, the macroscopic interface (the overall shape of the solidification front generated by the dendritic array, rather than the interface of an individual dendrite) diverges from a macroscopically flat interface into a concave or convex, curved interface [57].

4.2.1. Macroscopic interface curvature

General patterns of convective fluid motion corresponding to macroscopic curvature of the interface are shown schematically in Fig. 7, with relevance to the ice-templating system. Fig. 7(a), represents the ideal case where the macroscopic interface is flat. In Fig. 7(b), the solidification interface is convex; latent heat is preferentially evacuated through the solid, and the temperature at the edge of the sample is higher than the center. Most metallic alloys exhibit macroscopically convex interfaces as a result of higher thermal conductivities in the solid phase [60]. In the case of a

convex interface, convective fluid motion sweeps particles from the center of the interface to the sides, causing a build-up of particles at the mold walls. Conversely, in Fig. 7(c), convective fluid motion, reflective of a concave interface, sweeps particles radially inward, causing an accumulation of particles in the center of the solidification interface. In this case, there is a thermal conductivity mismatch at the junction of the mold, liquid, and/or solid, such that latent heat is evacuated at the interface radially, through the mold walls [60].

To elucidate the general pattern of convective motion in our samples, three samples were solidified under terrestrial conditions for each TiO_2 weight fraction. These samples were solidified identically to all other terrestrial samples except that, to prevent artificial disturbance of the interface shape, rubber plugs were not used to seal the top of the sample, and thus, the samples are not included in microstructural analysis. Care was taken to ensure the mold was filled evenly with the suspension, without scattering any of the colloid on the mold inner walls. A concave, "pit" depression [61] formed within the first 10 s of solidification and increased in depth over the course of solidification (~30 s). At conclusion of solidification, the average depth of the depression increased as the solid loading of the suspension increased, measuring *ca.* 1.1–1.2, 1.3–1.4, and 1.3–1.5 mm for the 8, 15, and 20 wt% TiO_2 suspensions, respectively.

The concave interface shape indicates a convective pattern consistent with Fig. 7(c), where latent heat is removed at the interface radially, *i.e.*, through the mold walls. However, the manufacturer's data for the PVC mold utilized lists the thermal conductivity as 0.19 W/m K. Neglecting effective thermal conductivity as a result of ceramic particle incorporation within the ice/colloid matrix and the colloid liquid, conductivity of the mold material remains significantly lower than that of ice (~2.2 W/m K) and water (0.6 W/m K). By these approximations, latent heat should be evacuated through the solid, which has higher thermal conductivity than both the liquid colloidal suspension and the mold material. Therefore, the concave curvature of the interface suggests that the thermal conductivity of the colloid is higher than the ice-particle composite.

Although not yet explored in ice-templating systems, nanoparticle-induced increased thermal conductivity of colloids is a growing field of research [62–64]. The theoretical basis of thermal conductivity enhancement in nanoparticle colloids relies on particle size-dependent Brownian motion [63], which is very high for nanometric particles. Indeed, only nanoparticles within the unsolidified colloid would offer enhancement to thermal conductivity because random motion is negligible for nanoparticles incorporated within the ice composite. Thus far, nanoparticle-enhanced thermal conductivity of colloids has primarily been studied for relatively low particle fractions (<1 to 5 vol% [63,64]), making it difficult to extend findings to the sufficiently higher particle fractions commonly employed in ice-templating systems.

The development of periodic ice lenses in the 20 wt% TiO_2 can be explained by the concave shape of the interface. With respect to the freezing direction, the ice lenses observed here are horizontally oriented layers consisting of alternating regions of planar ice (particle-free lenses) and concentrated particles/ice regions (Fig. 3), consistent with a cyclical pattern of particle engulfment. Ice-lenses are the most commonly observed defect in ice-templated materials and they significantly reduce the material's compressive strength [7]. In the ice lens arrays observed here, the particle fraction within the interface depression likely reached "breakthrough" concentration [8], wherein the osmotic pressure of the particle colloid exceeded the capillary pressure necessary to allow ice to invade the pore space. As shown by Barr and Luijten [65], particles can be engulfed when the velocity of the solidification front is below the critical velocity for engulfment (as it was here) if the particle fraction within the accumulation region is sufficiently high such that surrounding particles force particles nearest the interface into the ice front; it is likely that this scenario occurred in the present experiments.

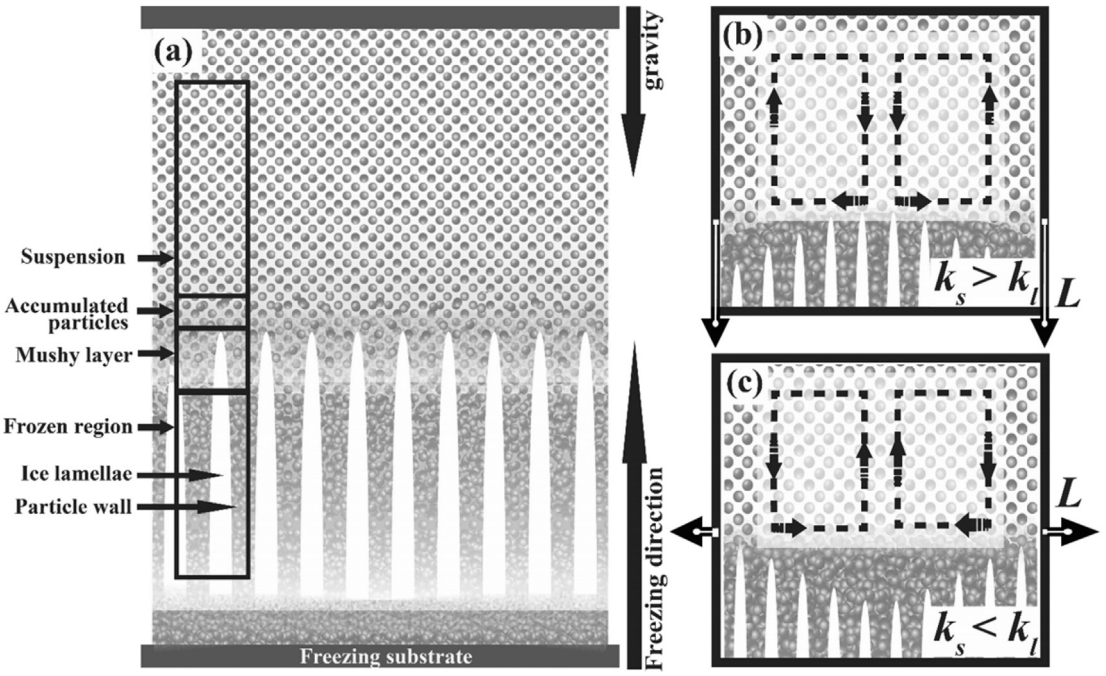

Fig. 7. Schematic of macroscopic interface curvature; freezing direction is vertically upwards. (a) is representative of a macroscopically planar interface; the particle fraction is relatively homogenous across the interface and convective fluid motion is limited to that driven by vertical concentration and temperature gradients. General convective fluid motion patterns associated with an (b) convex and (c) concave interface shape. Here, L is latent heat of fusion and k is thermal conductivity of the solid (s) or liquid (l).

The ratio of λ_L obtained under microgravity and terrestrial conditions ($\lambda_1^{\mu g}/\lambda_1^t$), which is ~2.3 at 5 wt% TiO_2, increases steadily with increasing TiO_2 weight fractions, reaching ~2.8 and ~3.3 at 8 and 15 wt% TiO_2, respectively. As the TiO_2 fraction increases, particle diffusion in the liquid becomes increasingly hindered. The boundary layer height (the height of the particle concentration gradient from the interface to the bulk liquid) is likewise reduced [66]. That is, the concentration gradient occurs over a smaller length scale because particles are not as free to diffuse away from the interface. The combination of a decrease in both boundary layer height and particle diffusion within the liquid offers less compensation for the downward component of fluid velocity that is driven by convection [57,67] and results in increased values of $\lambda_1^{\mu g}/\lambda_1^t$ [57].

A sharp decline in $\lambda_1^{\mu g}/\lambda_1^t$ is observed from ~3.3 at 15 wt% TiO_2 to ~2.2 at 20 wt% TiO_2 (Fig. 4(a)). At higher solid loadings, $\lambda_1^{\mu g}/\lambda_1^t$ converges for all values of gravitational acceleration. This can be explained by the macroscopically concave interface. After the concave shape develops, convective fluid motion sweeps particles radially from the mold walls toward the center of the interface. As solidification proceeds, the solid fraction within this region continues to increase resulting in a concomitant decrease in permeability within the region. As the accumulation region becomes less permeable, the downward component of interdendritic flow velocity resulting from convection [68] decreases and microgravity and terrestrial values of λ_L are observed to be in closer agreement than for any of the other particle fractions employed here.

It should be noted that any curvature of the liquid/solid interface resulting from even a slight increase in thermal conductivity of the colloid relative to the solid ice/particle composite is likely exacerbated as a result of the high solidification velocity employed here [61]. For situations in which a concave depression develops as a result of an unavoidable thermal conductivity mismatch, booster heaters, which inject heat at the solidification interface through the mold wall are commonly used to compensate for heat extraction during the solidification of organic metallic analogues [69,70] to control undesired interface curvature. A similar solution may offer a means to control interface curvature, and resulting convective fluid motion, for ice-templating systems.

4.3. Microgravity solidification of binary alloys

The solidification of metallic alloys [71] and organic analogues to metallic alloys [72] has been studied in microgravity for over thirty years to better understand the complex phenomena that govern solidification. Binary alloy solidification data under diffusion-controlled (*i.e.*, microgravity) environments are typically in good agreement with theoretical models describing λ_1. Conversely, systems that are influenced strongly by gravity-induced convection show large deviations from theoretical models when solidified under terrestrial conditions [73,74]. Increased values of $\lambda_1^{\mu g}/\lambda_1^t$ in alloys such as Al-Cu [68,73,75,76] and Al-Ni [57,77] is well documented in the literature and attributed to gravity-driven convective effects during solidification [57,68,73,75–82]. Values of $\lambda_1^{\mu g}/\lambda_1^t$ below unity are also reported in the literature for systems such as Al-7 wt% Si [83] alloys when solidified at relatively low solidification velocities and high thermal gradients (v = 0.87 μm/s, G = 15.8 K/mm; $\lambda_1^{\mu g}/\lambda_1^t$ = 0.96), and succinonitrile-0.24 wt% camphor [84] (organic metallic alloy analogue; v = 0.3–7 μm/s, G = 1.2–2.8 K/mm, with associated values of $\lambda_1^{\mu g}/\lambda_1^t$ ranging from 0.55 to 0.97, respectively).

Literature values of $\lambda_1^{\mu g}/\lambda_1^t$ in binary alloys are plotted in Fig. 8 against $v^{-1/4} \cdot G^{-1/2}$, based on Eq. (2). Two populations of data can be observed in Fig. 8: (1) non-metallic systems in which $\rho_{solute}/\rho_{solvent} \approx 1$ (SCN-Camphor [69] and SCN-Acetone [85]), and (2) metallic systems in which $\rho_{solute}/\rho_{solvent} \neq 1$ (Al-Cu [68,73,75,76,80], Al-Ni [57,77], Al-Si [78,83,86], Al-Li [81], Bi-Mn [87,88] Cu-Mn [82,85]). Linear regression lines are shown for each population, with the bottom and top lines corresponding respectively to: (1) $\rho_{solute}/\rho_{solvent} \approx 1$ ($y = 1.5x + 0.4$, $N = 13$, $r = 0.85$, $R^2 = 0.72$, $p < 0.001$, where $y = \lambda_1^{\mu g}/\lambda_1^t$ and x is the value corresponding to $v^{-1/4} \cdot G^{-1/2}$ from the Hunt and Lu [56] model of λ_1, N is number of observations, r is the correlation coefficient, R^2 is the coefficient of determination, and p is the calculated probability), and (2) $\rho_{solute}/\rho_{solvent} \neq 1$ ($y = 2.6x + 1.14$, $N = 24$, $r = 0.49$, $R^2 = 0.24$, $p = 0.014$). Less data scattering about the regression line is observed in systems where $\rho_{solute}/\rho_{solvent} \approx 1$, as compared to systems where $\rho_{solute}/\rho_{solvent} \neq 1$. Shaded regions about each regression line represent a 95% confidence interval.

Data from the present study are shown as black circles in Fig. 8. For all TiO_2-water data points shown in Fig. 8, the value of $v^{-1/4} \cdot G^{-1/2}$ is estimated to be 0.63. This estimate is based on a measured average solidification velocity of 100 μm/s and an estimated thermal gradient of 2.5 K/cm derived from *in-situ* temperature measurements of solidification of the TiO_2-water system under normal terrestrial gravity. As all TiO_2-water data points correspond to the same estimated x-value of $v^{-1/4} \cdot G^{-1/2} = 0.63$, data points for TiO_2-water are offset horizontally in Fig. 8, within the estimated error range of $v^{-1/4} \cdot G^{-1/2}$, to enable visualization of error bars corresponding to the individual points. These TiO_2-water data are provided for comparison to microgravity alloy solidification only and

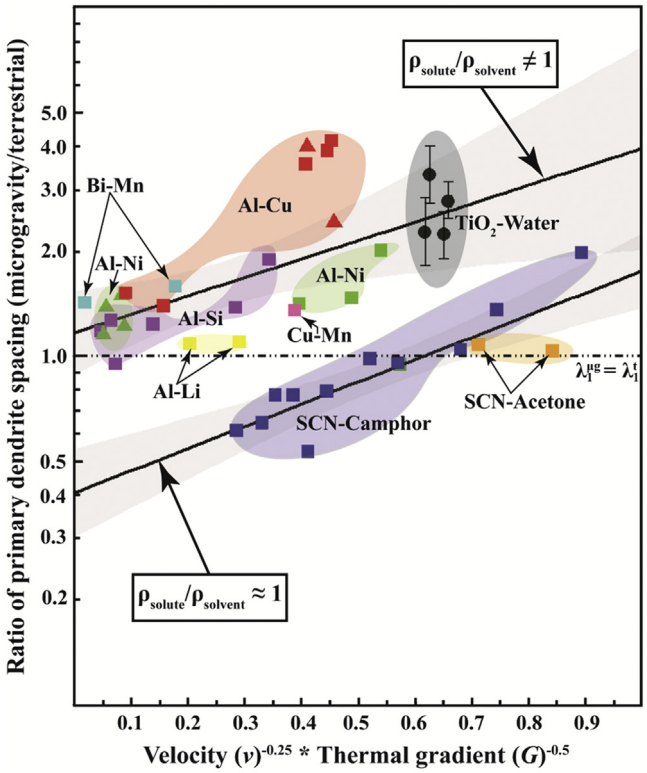

Fig. 8. Plot of literature data reporting ratio of primary dendrite spacing obtained under microgravity ($\lambda_1^{\mu g}$) and terrestrial (λ_1^t) conditions (defined as: $\lambda_1^{\mu g}/\lambda_1^t$) as a function of $v^{-1/4} \cdot G^{-1/2}$. Hyper- and hypoeutectic systems are shown in triangles and squares, respectively. Present data are shown as black circles and are offset horizontally within the estimated error range of $v^{-1/4} \cdot G^{-1/2}$, to ease visibility of error bars. Regression lines correspond to: (i) metallic systems where $\rho_{solute}/\rho_{solvent} \neq 1$ (Al-Cu [68,73,75,76,80], Al-Ni [57,77], Al-Si [78,83,86], Al-Li [81], Bi-Mn [87,88], Cu-Mn [82], and (ii) non-metallic systems where $\rho_{solute}/\rho_{solvent} \approx 1$ (SCN-Camphor [69] and SCN-Acetone [85]. Shaded regions about each regression line represent 95% confidence intervals.

were not included in linear regression analysis. Interestingly, these data are in good agreement with the regression line that corresponds to the $\rho_{solute}/\rho_{solvent} \neq 1$ alloy systems.

Systems in which $\rho_{solute}/\rho_{solvent} \approx 1$, show less dependence of λ_1 on gravity-induced convection ($\lambda_1^{\mu g}/\lambda_1^t$: mean ($M$) = 0.97, standard deviation (SD) = 0.15, N = 13) than systems where $\rho_{solute}/\rho_{solvent} \neq 1$, which show significantly increased values of $\lambda_1^{\mu g}/\lambda_1^t$ ($\lambda_1^{\mu g}/\lambda_1^t$: M = 1.8, SD = 0.9, N = 24; two-sample t-test for unequal variances, $t(33) = -3.88$, $p < 0.001$). However, a difference in $\lambda_1^{\mu g}/\lambda_1^t$ between systems where $\rho_{solute}/\rho_{solvent} < 1$, and >1, is not observed, suggesting a potential dependence of $\lambda_1^{\mu g}/\lambda_1^t$ on the existence of a density difference between $\rho_{solute}/\rho_{solvent}$, independent of direction. Indeed, Al-Si and Al-Ni show a similar dependence of $v^{-1/4} \cdot G^{-1/2}$ on $\lambda_1^{\mu g}/\lambda_1^t$, as shown in Fig. 7, despite having a $\rho_{solute}/\rho_{solvent}$ value of 0.86 and 3.3, respectively.

Differences in $\lambda_1^{\mu g}/\lambda_1^t$ are likewise, not observed between hypo- and hypereutectic alloys (shown in Fig. 8, as squares and triangles, respectively), which differ with regard to the interface solute concentration relative to the bulk. Consider the case of the Al-Cu alloys, which, in addition to having the largest values of $\lambda_1^{\mu g}/\lambda_1^t$, have a higher density mismatch between solute and solvent than any of the other systems ($\rho_{solute}/\rho_{solvent}$ = 3.3). The cluster of five Al-Cu data points shown in Fig. 8 correspond to three hypoeutectic alloys of 20 [68] and 26 wt% Cu [68,76] (red squares) and two hypereutectic alloys at 38 [73] and 40 [68] wt% Cu (red triangles), with the 40 wt% having the lowest value of $\lambda_1^{\mu g}/\lambda_1^t$ at 2.4.

Hypoeutectic Al-Cu alloys exhibit similar solute redistribution behavior as described for the ice-templating system, wherein Cu solute accumulates ahead of the interface, leading to a higher concentration of Cu at the interface relative to the bulk liquid. In hypoeutectic Al-Cu systems, the fluid density at the interface is greater than the bulk due to the higher concentration of Cu. Conversely, in hypereutectic systems, the interface is solvent- (Al-) rich, and therefore, less dense than the bulk fluid. Despite the differences in density at the interface vs. the bulk, values of $\lambda_1^{\mu g}/\lambda_1^t$ are in good agreement between the 20 and 26 wt% hypoeutectic and the 38 wt% hypereutectic alloys. This is especially the case for the hypoeutectic 26 wt% [68] and hypereutectic 38 wt% [73] Cu, both solidified under similar values of $v^{-1/4} \cdot G^{-1/2}$ in long-term microgravity environment, having similar values of $\lambda_1^{\mu g}/\lambda_1^t$ of 3.4 and 3.9, respectively.

The steady-state boundary layer height δ, which is an approximation of the height of the concentration gradient from the interface to the bulk concentration [66], is taken as:

$$\delta = 2D_L/v \tag{3}$$

where D_L is the diffusion coefficient of solute in the liquid and v is the solidification velocity. By Eq. (3), the boundary layer height is estimated to be substantially lower for the hypereutectic Al-Cu alloy compared to that of the hypoeutectic (δ = 0.38 and 1.33 μm, respectively), meaning that the concentration gradient occurs over a smaller length scale in the alloy with a higher value of $\lambda_1^{\mu g}/\lambda_1^t$, which is consistent with the explanation offered for the increase in values of $\lambda_1^{\mu g}/\lambda_1^t$ for 15 vs. 5 wt% TiO_2 observed here.

4.4. Relating microgravity alloy solidification to ice-templating

The microgravity time restrictions of parabolic flight only allow for ~30 s of solidification time per sample. To maximize sample depth, solidification velocities explored here (100 μm/s) were the highest velocities attainable using the dry ice-cooled copper substrate. As such, a range of velocities were not explored and a value for n from Eq. (1), cannot be calculated. As we have shown, gravity-driven convective effects reduce λ_1 in binary alloys, particularly when $\rho_{solute}/\rho_{solvent} \neq 1$, consistent with the results reported here for TiO_2 colloid solidification. A limitation of this study is that microstructural data was obtained from sintered samples. Although a statistically significant difference between microgravity and terrestrial sample shrinkage could not be detected, it is known that sintering shrinkage can alter the templated microstructure in freeze-cast materials [89].

To explore whether the concept that gravity-driven convection decreases λ_L as observed here, can be generalized to other ice-templating systems, literature data are utilized from ice-templating studies of sintered, green, and green samples filled with epoxy, as well as *in situ* investigations, to determine if λ_L shows a similar dependency on the ratio of particle-to-fluid density (ρ_p/ρ_f) as observed in microgravity solidification of binary alloy systems. Data from studies employing water as the fluid and reporting v and λ_L are shown in Fig. 9, for aqueous suspensions of: (a) lanthanum strontium manganite/yttria-stabilized zirconia (LSM-YSZ) [90]; (b) Al_2O_3 [18,21,34,49,50,91–94], SiC [95], tricalcium phosphate (TCP) [96,97], Si [98]; (c) SiO_2 [99–101] and collagen [10]; and (d) tert-butyl alcohol (TBA) [102] and acetic acid (HAc) [10]. Systems containing lower density particles (collagen, SiO_2) or solute (TBA, HAc) than water show a weaker overall dependence of λ_L on solidification velocity when compared to systems consisting of higher density particles (LSM-YSZ, Al_2O_3, TCP, SiC, Si).

A least squares regression is utilized to obtain a value of n from Eq. (1), for each particle system. Fig. 9(e) shows the n values obtained plotted against ρ_p/ρ_f; statistical significance was obtained for all slope coefficient values with the exception of acetic acid (HAc) and tert-Butyl alcohol (TBA). All regression statistics are provided in Table 2.

Excluding HAc and TBA, an inverse relationship between n and ρ_p/ρ_f is still observed as can be inferred by comparing consecutive plots from Fig. 9(a)–(c); the slope of each regression line increases as the magnitude of ρ_p/ρ_f decreases. Values of n as deduced from Fig. 8(a–e), are plotted against relative density values ρ_p/ρ_f for each system. Linear regression analysis is utilized to obtain the line depicted in Fig. 9(e) ($y = -0.23x + 0.13$, $r = 0.93$, $R^2 = 0.86$, $N = 7$, $p = 0.002$). The relationship depicted between n and ρ_p/ρ_f shown in Fig. 9(e) is simplified as factors such as solid particle fraction and size, among others, are not accounted for. Nevertheless, a clear relationship between n and ρ_p/ρ_f is observed. By Eq. (1), this suggests that systems with a relatively higher ratio of ρ_p/ρ_f have a greater dependence of λ_L on v. An empirical dependence of λ_L on the ratio, ρ_p/ρ_f, coupled with the experimental results presented here, is highly suggestive that gravity-driven convective effects influence λ_L in ice-templating systems. Additional microgravity investigations in a longer term microgravity environment, enabling experiments at a range of solidification velocities, are necessary to clarify this relationship.

5. Conclusions

This study addresses the role of gravity-driven convection on microstructural formation during directional solidification of aqueous suspensions of 5–20% wt% nanometric titanium dioxide (TiO_2) particles. These suspensions were solidified under reduced (micro-, lunar, Martian) gravitational conditions during ~25 s reduced gravity periods on parabolic flights as well as under normal terrestrial gravitational conditions, as the first step of an ice-templating process. As a result of an induced thermal gradient, ice dendrites grow perpendicular to the freezing surface, rejecting particles from the advancing front and later forcing assembly within interdendritic space. After solidification, the ice dendrites were removed by sublimation and the resulting TiO_2 samples were sintered to densify particle-packed walls aligned with the

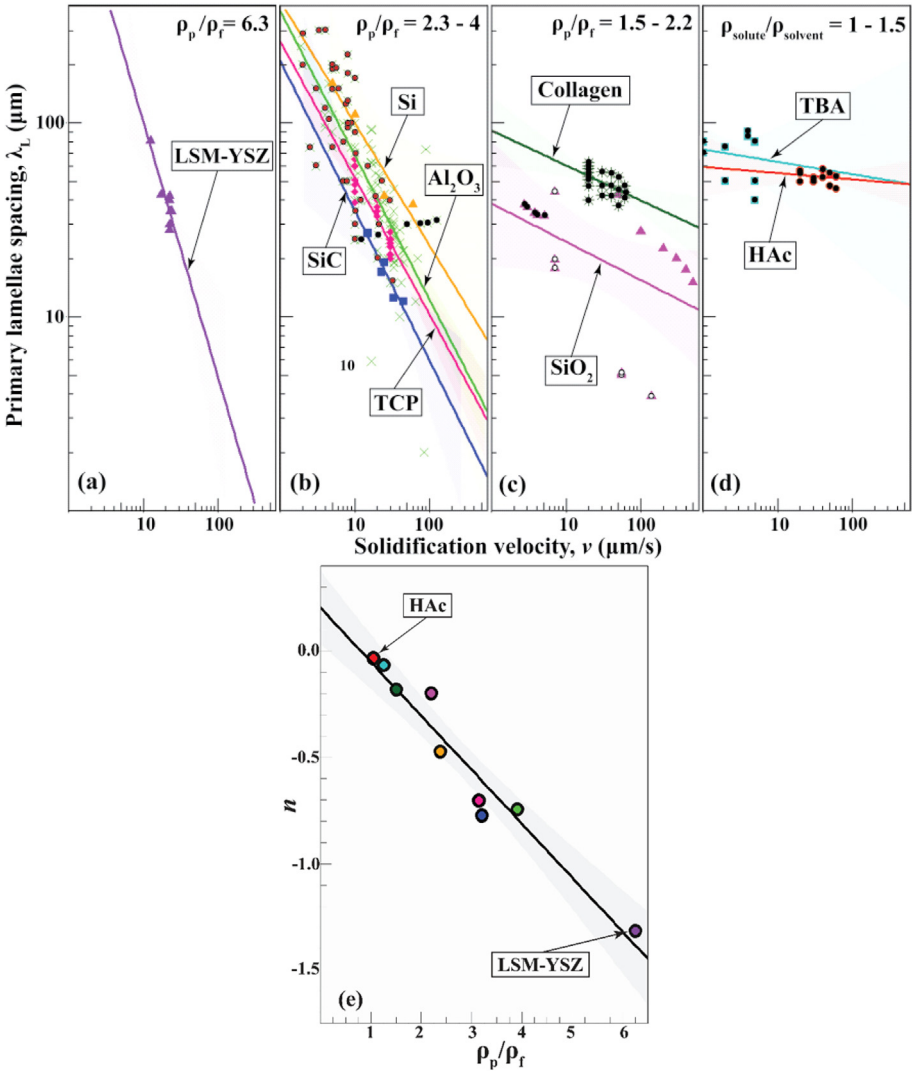

Fig. 9. Plot of lamellae spacing λ_L vs. solidification velocity v for literature data on aqueous suspensions of: (a) LSM-YSZ [90], (b) Al_2O_3 [18,21,34,49,50,91–94], SiC [95], TCP [96,97], Si [98], (c) SiO_2 [99–101], and Collagen [10], and (d) TBA [102], and HAc [10]. Data obtained during *in situ* investigations, microstructural analysis of green bodies and green bodies whose pores were filled with epoxy are shown in black circles, white and red circles with black outlines, respectively; data obtained from sintered samples contain no additional marking. Lines are linear regression of data; shaded regions represent 95% confidence intervals. (e) Plot of n (calculated from (a) as Eq. (1)) vs. relative density ratio (ρ_p/ρ_L); colors of plot points on (e) correspond to systems shown in (a) through (d). (For interpretation of the references to colour in this figure legend, the reader is referred to the web version of this article.)

Table 2
Summary of least square regression statistics and calculated n values from Eq. (1), for literature values reporting solidification velocity (v) and lamellae spacing (λ_L) as plotted in Fig. 9(a–d); correlation coefficient (r), number of data points (N), degrees of freedom (*d.f.*), and probability value (p). The density ratio of particle/fluid (ρ_p/ρ_f) utilized for each system plotted in Fig. 9(e) is also provided.

System	Reference(s)	ρ_p/ρ_f	n	r	N	*d.f.*	p
LSM-YSZ/Water	[90]	6.5	−1.316	0.79	8	6	0.003
Al_2O_3/Water	[18,21,34,49,50,91–94]	3.9	−0.74	0.61	129	127	<0.0001
TCP/Water	[96,97]	3.0	−0.704	0.85	20	18	<0.0001
SiC/Water	[95]	3.2	−0.77	0.91	5	3	0.01
SiO_2/Water	[99–101]	2.7	−0.20	0.23	17	15	0.049
Si/Water	[98]	2.3	−0.47	0.92	4	2	0.04
Collagen/Water	[10]	1.5	−0.18	0.30	24	22	0.005
Water/TBA	[102]	1.2	−0.06	0.02	12	10	0.6
HAc/Water	[10]	1.0	−0.03	0.04	15	13	0.5

temperature gradient.

Microstructural analysis of the sintered samples reveals a dependency of ice lamellae spacing (λ_L; analogous to interdendritic spacing in alloy solidification) on (i) TiO_2 weight fraction and (ii) gravitational acceleration. Increasing the TiO_2 fraction in the suspensions leads to decreased lamellar spacing in all samples, regardless of gravitational acceleration. Increasing the fraction of TiO_2 from 5 to 20 wt% decreases λ_L by a factor of ~3.5 in both

microgravity and terrestrial samples. For all solid loadings studied, λ_L is highest under microgravity conditions and reduces with increasing gravitational accelerations; at 15 wt% TiO_2, from ~0 to 1 g, λ_L decreases by a factor of ~3. This effect is less pronounced at higher solid loading fractions wherein λ_L decreases by a factor of 2, from 0 to 1 g, for the 20 wt% TiO_2. This is expected to be a direct result of reduced convective mixing at higher particle weight fractions resulting from decreased permeability within a region of accumulated particles, located ahead of the solidification interface.

Periodic ice lens structures interspersed between particle-packed beds oriented parallel to the solidification direction, unlike lamellae, which are oriented perpendicular to the freezing, are observed in two of the eight 20 wt% TiO_2 colloids solidified under terrestrial gravitational conditions, but not in any of the 32 samples solidified under reduced gravity (including eight samples with 20 wt% TiO_2) or for any of the lower solid loadings, independent of gravity values. Ice lenses in terrestrial samples are consistent with a pattern of particle engulfment.

Results of this study are in good agreement with previous microgravity studies of binary metallic alloy solidification. This suggests that solidification models of primary dendrite spacing, where solute is rejected at the interface by advancing dendrites, and experimental work on alloy solidification in microgravity is relevant to the solidification behavior of directionally-solidified aqueous colloids. Long-term microgravity studies are necessary to clarify these relationships.

Literature data from ice-templating studies are utilized to investigate a potential dependence of particle-to-fluid density on λ_L in ice-templated materials; an empirical power law relationship between λ_L and solidification velocity is confirmed. It is suggested that the particle-to-fluid density ratio is partially responsible for this dependence.

Acknowledgments

This work was supported by grants from NASA Flight Opportunities Program (NASA FOP), the Institute for Sustainability and Energy at Northwestern, Northwestern University (NU) Office of the Provost, and the Illinois Space Grant Consortium. This work made use of the MatCI Facility, and the J.B. Cohen X-Ray Diffraction Facility at Northwestern University (NU) which are supported by the MRSEC program of the National Science Foundation (DMR-1121262) at the Materials Research Center at NU. The authors thank the following NU students: Ms. Felicia Teller and Ms. Kimberly Clinch for their assistance during parabolic flight testing and Mr. Matthew Ocana for his assistance with ceramographic sample preparation. The authors also thank Mr. Robert Roe (NASA FOP) for his technical guidance during, and in preparation of, parabolic flight testing, Prof. M. Grae Worster (University of Cambridge) for his insight on ice banding, and Prof. Peter Voorhees (NU) for numerous useful discussions and helpful insights on alloy solidification.

References

[1] S. Deville, Freeze-casting of porous ceramics: a review of current achievements and issues, Adv. Eng. Mater. 10 (2008) 155–169.
[2] S. Deville, Freeze-casting of porous biomaterials: structure, properties and opportunities, Mater 3 (2010) 1913–1927.
[3] S. Deville, Ice-templating, freeze casting: beyond materials processing, J. Mater. Res. 28 (2013) 2202–2219.
[4] M. Gutierrez, M. Ferrer, F. del Monte, Ice-templated materials: sophisticated structures exhibiting enhanced functionalities obtained after unidirectional freezing and ice-segregation-induced self-assembly, Chem. Mater. 20 (2008) 634–648.
[5] R. Liu, T. Xu, C. Wang, A review of fabrication strategies and applications of porous ceramics prepared by freeze-casting method, Ceram. Int. 42 (2016) 2907–2925.
[6] K.M. Pawelec, A. Husman, S.M. Best, R.E. Cameron, Ice-templated structures for biomedical tissue repair: from physics to final scaffolds, Appl. Phys. Rev. (2014) 1.
[7] S. Deville, S. Meille, J. Seuba, A Meta-analysis of the mechanical properties of ice-templated ceramics and metals, Sci. Technol. Adv. Mater. (2016).
[8] N.O. Shanti, K. Araki, J.W. Halloran, Particle redistribution during dendritic solidification of particle suspensions, J. Am. Ceram. Soc. 89 (2006) 2444–2447.
[9] T. Fukasawa, Z.Y. Deng, M. Ando, Pore structure of porous ceramics synthesized from water-based slurry by freeze-dry process, J. Mater. Sci. 36 (2001) 2523–2527.
[10] H. Schoof, L. Bruns, A. Fischer, I. Heschel, G. Rau, Dendritic ice morphology in unidirectionally solidified collagen suspensions, J. Cryst. Growth 209 (2000) 122–129.
[11] Y. Chino, D.C. Dunand, Directionally freeze-cast titanium foam with aligned, elongated pores, Acta Mater. 56 (2008) 105–113.
[12] A. Szepes, J. Ulrich, Z. Farkas, J. Kovacs, P. Szabo-Revesz, Freeze-casting technique in the development of solid drug delivery systems, Chem. Eng. Prog. 46 (2007) 230–238.
[13] A. Witte, J. Ulrich, An alternative technology to form tablets, Chem. Eng. Technol. 33 (2010) 757–761.
[14] P.T.N. Nguyen, J. Ulrich, Fast dispersible cocoa tablets: a case study of freeze-casting applied to foods, Chem. Eng. Technol. 37 (2014) 1376–1382.
[15] P.T.N. Nguyen, J. Ulrich, Sugar alcohols - multifunctional agents in the freeze casting process of foods, J. Food Eng. 153 (2015) 1–7.
[16] U.G.K. Wegst, M. Schecter, A. Donius, P.M. Hunger, Biomaterials by freeze casting, Philos. Trans. R. Soc. Math. Phys. Eng. Sci. 368 (2010) 2099–2121.
[17] Y. Zhang, K. Zhou, J. Zeng, D. Zhang, Control of pore structures and sizes in freeze cast ceramics, Adv. Appl. Sci. 112 (2013) 405–411.
[18] T. Waschkies, R. Oberacker, M.J. Hoffmann, Investigation of structure formation during freeze-casting from very slow to very fast solidification velocities, Acta Mater. 59 (2011) 5135–5145.
[19] F. Ye, J. Zhang, L. Liu, H. Zhan , Effect of solid content on pore structure and mechanical properties of porous silicon nitride ceramics produced by freeze casting, Mater. Sci. Eng. A Struct 528 (2011) 1421–1424.
[20] C. Pekor, B. Groth, I. Nettleship, The effect of polyvinyl alcohol on the microstructure and permeability of freeze-cast alumina, J. Am. Ceram. Soc. 93 (2010) 115–120.
[21] C. Pekor, B. Groth, I. Nettleship, Effect of polyethylene glycol on the microstructure of freeze-cast alumina, J. Am. Ceram. Soc. 91 (2008) 3185–3190.
[22] Y. Wu, J. Zhao, Y. Li, K. Lu, Preparation and freezing behavior of TiO 2 nanoparticle suspensions, Ceram. Int. 42 (2016) 15597–15602.
[23] K.M. Pawelec, A. Husmann, S.M. Best, R.E. Cameron, Understanding anisotropy and architecture in ice-templated biopolymer scaffolds, Mater. Sci. Eng. C Mater. Biol. Appl. 37 (2014) 141–147.
[24] S.S.L. Peppin, J.A.W. Elliott, M.G. Worster, Solidification of colloidal suspensions, J. Fluid Mech. 554 (2006) 147–166.
[25] M. Worster, Solidification of fluids, Perspect. Fluiddyn. 742 (2000) 393–446.
[26] Y.M.F. El Hasadi, J.M. Khodadadi, Numerical simulation of solidification of colloids inside a differentially heated cavity, J. Heat. Trans. T ASME (2015) 137.
[27] B. Delattre, H. Bai, R.O. Ritchie, J. De Coninck, A. Tomsia, Unidirectional freezing of ceramic suspensions: in situ X-ray investigation of the effects of additives, ACS Appl. Mater. Interfaces 6 (2014) 159–166.
[28] M. Bettge, H. Niculescu, P. Gielisse, Engineered porous ceramics using a directional freeze-drying process, in: 28th Int. Spring Semin. Elect. Technol.: IEEE, 2005, pp. 28–34.
[29] S.S.L. Peppin, M.G. Worster, J.S. Wettlaufer, Morphological instability in freezing colloidal suspensions, Proc. Math. Phys. Eng. Sci. 463 (2007) 723–733.
[30] K. Nakagawa, N. Thongprachan, T. Charinpanitkul, W. Tanthapanichakoon, Ice crystal formation in the carbon nanotube suspension: a modelling approach, Chem. Eng. Sci. 65 (2010) 1438–1451.
[31] R. Owen, M. Johnston, Optical observations of unidirectional solidification and related fluid parameters in microgravity, Opt. Laser Eng. 5 (1984) 95–108.
[32] N. Otsu, A threshold selection method from gray-level histograms, Automatica 11 (1975) 23–27.
[33] K. Zuiderveld, Contrast Limited Adaptive Histogram Equalization. Graphics Gems IV, Academic Press Professional, Inc., 1994, pp. 474–485.
[34] S. Deville, E. Saiz, A. Tomsia, Ice-templated porous alumina structures, Acta Mater. 55 (2007) 1965–1974.
[35] J.S. Pontius, Estimation of the mean in line intercept sampling, Environ. Ecol. Stat. 5 (1998) 371–379.
[36] S. Fazio, J. Guzman, M. Colomer, A. Salomoni, R. Moreno, Colloidal stability of nanosized titania aqueous suspensions, J. Eur. Ceram. Soc. 28 (2008) 2171–2176.
[37] R.N. Grugel, L.N. Brush, A.V. Anilkumar, Disruption of an aligned dendritic network by bubbles during re-melting in a microgravity environment, Microgravity Sci. Technol. 24 (2012) 93–101.
[38] D.A. Hanaor, C.C. Sorrell, Review of the anatase to rutile phase transformation, J. Mater. Sci. 46 (2011) 855–874.
[39] L. Ren, Y.P. Zeng, D. Jiang, Preparation of porous TiO2 by a novel freeze casting, Ceram. Int. 35 (2009) 1267–1270.
[40] L. Ren, Y.P. Zeng, D. Jiang, Fabrication of gradient pore TiO2 sheets by a novel freeze–tape-casting process, J. Am. Ceram. Soc. 90 (2007) 3001–3004.

[41] A.M. Anderson, M.G. Worster, Periodic ice banding in freezing colloidal dispersions, Langmuir 28 (2012) 16512–16523.
[42] A.M.G. Anderson, M.G. Worster, Freezing colloidal suspensions: periodic ice lenses and compaction, J. Fluid Mech. 758 (2014) 786–808.
[43] K. Watanabe, Relationship between growth rate and supercooling in the formation of ice lenses in a glass powder, J. Cryst. Growth 237 (2002) 2194–2198.
[44] S. Deville, S. Meille, J. Seuba, A meta-analysis of the mechanical properties of ice-templated ceramics and metals, Sci. Technol. Adv. Mater. (2016).
[45] S. Peppin, A. Majumdar, R. Style, G. Sander, Frost heave in colloidal soils, SIAM J. Appl. Math. 71 (2011) 1717–1732.
[46] J.M.H. Schollick, R.W. Style, A. Curran, J.S. Wettlaufer, E.R. Dufresne, P.B. Warren, et al., Segregated ice growth in a suspension of colloidal particles, J. Phys. Chem. B (2016).
[47] R.W.P. Style, S.L. Peppin, The kinetics of ice-lens growth in porous media, J. Fluid Mech. 692 (2012) 482–498.
[48] J. You, J. Wang, L. Wang, Z. Wang, J. Li, X. Lin, Formation Mechanism of Ice Banding in Freezing Colloidal Suspensions, arXiv preprint arXiv:1605.03802, 2016.
[49] S. Miller, X. Xiao, K. Faber, Freeze-cast alumina pore networks: effects of freezing conditions and dispersion medium, J. Eur. Ceram. Soc. 35 (2015) 3595–3605.
[50] R. Oberacker, T. Waschkies, M. Hoffmann, Microstructure maps for unidirectional freezing of particle suspensions, Adv. Process. Manuf. Technol. Struct. Multifunct. Mater. V 32 (2011) 35–44.
[51] M. Spannuth, S.G.J. Mochrie, S.S.L. Peppin, J.S. Wettlaufer, Particle-scale structure in frozen colloidal suspensions from small-angle x-ray scattering, Phys. Rev. E (2011) 83.
[52] S. Deville, E. Maire, G. Bernard-Granger, A. Lasalle, A. Bogner, C. Gauthier, J. Leloup, C. Guizard, Metastable and unstable cellular solidification of colloidal suspensions, Nat. Mater. 8 (2009) 966–972.
[53] R. Trivedi, Interdendritic spacing: Part II. A comparison of theory and experiment, Metall. Trans. A 15 (1984) 977–982.
[54] J.D. Hunt, Pattern formation in solidification, Mater. Sci. Technol. 15 (1999) 9–14.
[55] P. Lehmann, R. Moreau, D. Camel, R. Bolcato, A simple analysis of the effect of convection on the structure of the mushy zone in the case of horizontal Bridgman solidification. Comparison with experimental results, J. Cryst. Growth 183 (1998) 690–704.
[56] J. Hunt, S.-Z. Lu, Numerical modeling of cellular/dendritic array growth: spacing and structure predictions, Metall. Mater. Trans. A 27 (1996) 611–623.
[57] H.N. Thi, Y. Dabo, B. Drevet, M.D. Dupouy, D. Camel, B. Billia, et al., Directional solidification of Al-1.5 wt% Ni alloys under diffusion transport in space and fluid-flow localisation on earth, J. Cryst. Growth 281 (2005) 654–668.
[58] R. Trivedi, H. Miyahara, P. Mazumder, E. Simsek, S. Tewari, Directional solidification microstructures in diffusive and convective regimes, J. Cryst. Growth 222 (2001) 365–379.
[59] S. Roper, S. Davis, P. Voorhees, Localisation of convection in mushy layers by weak background flow, J. Fluid Mech. 675 (2011) 518–528.
[60] P. Mazumder, R. Trivedi, Integrated simulation of thermo-solutal convection and pattern formation in directional solidification, Appl. Math. Model. 28 (2004) 109–125.
[61] C.W. Lan, C.Y. Tu, Morphological instability due to double diffusive convection in directional solidification: the pit formation, J. Cryst. Growth 220 (2000) 619–630.
[62] S. Chol, Enhancing thermal conductivity of fluids with nanoparticles, ASME Publ. Fed. 231 (1995) 99–106.
[63] S.P. Jang, S.U. Choi, Role of brownian motion in the enhanced thermal conductivity of nanofluids, Appl. Phys. Lett. 84 (2004) 4316–4318.
[64] S. Murshed, K. Leong, C. Yang, Enhanced thermal conductivity of TiO2—-water based nanofluids, Int. J. Therm. Sci. 44 (2005) 367–373.
[65] S.A. Barr, E. Luijten, Structural properties of materials created through freeze casting, Acta Mater. 58 (2010) 709–715.
[66] D.M. Stefanescu, Solidification of Metal Matrix Composites. Science and Engineering of Casting Solidification, Springer, 2015, pp. 305–341.
[67] S. Kaddeche, J. Garandet, C. Barat, H.B. Hadid, D. Henry, Interface curvature and convection related macrosegregation in the vertical Bridgman configuration, J. Cryst. Growth 158 (1996) 144–152.
[68] M. Dupouy, D. Camel, J. Favier, Natural convective effects in directional dendritic solidification of binary metallic alloys: dendritic array primary spacing, Acta Metall. Mater. 40 (1992) 1791–1801.
[69] N. Bergeon, F. Mota, L. Chen, D. Tourret, J. Debierre, R. Guérin, et al., Dynamical microstructure formation in 3D directional solidification of transparent model alloys: in situ characterization in DECLIC directional solidification insert under diffusion transport in microgravity, in: IOP Conf. Ser. Mater. Sci. Eng., IOP Publishing, 2015, p. 012077.
[70] A. Weiss, L. Sturz, G. Zimmermann, Investigation on the morphological instability during directional solidification of a transparent alloy during sounding rocket flights, in: R. Roosz, M. Rettenmayr, Z. Gacsi (Eds.), Solidification and Gravity IV, 2006, pp. 463–471.
[71] J.D. Thompson, E.B. Gulsoy, P.W. Voorhees, Self-similar coarsening: a test of theory, Acta Mater. 100 (2015) 282–289.
[72] M. Glicksman, M.B. Koss, E.A. Winsa, Dendritic growth velocities in microgravity, Phys. Rev. Lett. 73 (1994) 573.
[73] H. Yu, K.N. Tandon, J.R. Cahoon, Solidification of hypereutectic Al-38 wt pct Cu alloy in microgravity and in unit gravity, Metall. Trans. A 28 (1997) 1245–1250.
[74] H.M. Tensi, R. Rosch, Interdendritic eutectic solidification of an ALSI-7.0 alloy under microgravity, Metall. Trans. B 24 (1993) 208–212.
[75] J. Favier, J. Berthier, P. Arragon, Y. Malmejac, V. Khryapov, I. Barmin, Solid/liquid interface stability in normal and microgravity conditions: the ELMA 01 experiments, Acta Astronaut. 9 (1982) 255–259.
[76] D. Camel, M. Dupouy, J. Favier, R. Le Maguet, Preliminary results of the D1-WL-GHF-04 experiment on dendritic solidification of Al-Cu alloys, Adv. Space Res. 6 (1986) 127–132.
[77] N. Zhang, X. Luo, S. Feng, Y. Ren, Mechanism of gravity effect on solidification microstructure of eutectic alloy, J. Mater. Sci. Technol. 30 (2014) 499–503.
[78] S. Angart, M. Lauer, S. Tewari, R. Grugel, D. Poirier, Comparison of Directionally Solidified Samples Solidified Terrestrially and Aboard the International Space Station, NASA Tech. Rep., 2014.
[79] F. Barbieri, C. Patuelli, Eutectic structures of Ag-Cu after melting and solidification in microgravity and on Earth, Metall. Trans. A 19 (1988) 2659–2664.
[80] J. Cahoon, M. Chaturvedi, K. Tandon, The unidirectional solidification of Al-4 wt pct Cu ingots in microgravity, Metall. Trans. A 29 (1998) 1101–1111.
[81] B. Drevet, H.N. Thi, D. Camel, B. Billia, M.D. Dupouy, Solidification of aluminium-lithium alloys near the cell/dendrite transition-influence of solutal convection, J. Cryst. Growth 218 (2000) 419–433.
[82] G. Zimmermann, A. Weiss, Directional solidification of dendritic microstructures in microgravity and with forced melt flow, Microgravity Sci. Technol. 16 (2005) 143–147.
[83] H.M. Tensi, Influence of microgravity on the morphology of the directionally solidified front in an AlSi alloy, Metall. Trans. A 19 (1988) 2681–2686.
[84] L. Chen, Dynamical Microstructure Formation in 3D Directional Solidification of Transparent Model Alloys: in Situ Characterization in DECLIC-DSI under Diffusion Transport in Microgravity, Aix-Marseille, 2013.
[85] A.H. Weiss, G. Zimmermann, S. Rex, S. Coriell, Investigation on morphological instability during directional solidification on a sounding rocket, Mater. Sci. Forum (2000) 277–284. Trans Tech Publ.
[86] S. Steinbach, L. Ratke, H.D. Masslow, Directional solidification of binary AlSi-alloys in diffusive and convective regimes, in: 17th ESA Symposium on European Rocket and Balloon Programmes and Related Research, 2005, pp. 521–526.
[87] R.G. Pirich, D. Larson, Influence of gravity driven convection on the directional solidification of Bi/MnBi eutectic composites, in: MRS Proc., Cambridge Univ Press, 1981, p. 523.
[88] R.G. Pirich, D. Larson Jr., SPAR VI Technical Report for Experiment 76-22: Directional Solidification of Magnetic Composites, NASA Tech. Rep., 1980.
[89] A. Röthlisberger, S. Häberli, R. Spolenak, D. Dunand, Synthesis, structure and mechanical properties of directionally freeze-cast tungsten foams, J. Mater. Res. 31 (06) (2016) 753–764.
[90] A.Z. Lichtner, D. Jauffres, C.L. Martin, R.K. Bordia, Processing of hierarchical and anisotropic porosity LSM-YSZ composites, J. Am. Ceram. Soc. 96 (2013) 2745–2753.
[91] S. Deville, E. Maire, A. Lasalle, A. Bogner, C. Gauthier, J. Leloup, C. Guizard, In Situ X-ray radiography and tomography observations of the solidification of aqueous alumina particles suspensions. Part II: steady state, J. Am. Ceram. Soc. 92 (2009) 2497–2503.
[92] E.S. Gutierrez, M. Reece, N. Grobert, Bio-Inspired Ceramic/Carbon Composites, DTIC Document, 2012.
[93] C. Walter, S. Barg, N. Ni, R.C. Maher, E.G. Tunon, M. Ismail, F. Babot, E. Saiz , A novel approach for the fabrication of carbon nanofibre/ceramic porous structures, J. Eur. Ceram. Soc. 33 (2013) 2365–2374.
[94] T. Waschkies, R. Oberacker, M. Hoffmann, Control of lamellae spacing during freeze casting of ceramics using double-sided cooling as a novel processing route, J. Am. Ceram. Soc. 92 (2009) S79–S84.
[95] V.B. Naglieri, A. Hrishikesh, B. Gludovatz, A.P. Tomsia, R.O. Ritchie, On the development of ice-templated silicon carbide scaffolds for nature-inspired structural materials, Acta Mater. 61 (2013) 6948–6957.
[96] S. Flauder, U. Gbureck, F.A. Müller, β-TCP scaffolds with an interconnected and aligned porosity fabricated via ice-templating, Key Eng. Mater. (2013) 129–132. Trans Tech Publ.
[97] S. Flauder, U. Gbureck, F.A. Müller, Structure and mechanical properties of β-TCP scaffolds prepared by ice-templating with preset ice front velocities, Acta Biomater. 10 (2014) 5148–5155.
[98] D.S. Kim, D.K. Kim, Hierarchical structure of porous silicon nitride ceramics with aligned pore channels prepared by ice-templating and nitridation of silicon powder, Int. J. Appl. Ceram. Technol. (2015).
[99] S. Deville, J. Adrien, E. Maire, M. Scheel, M. Di Michiel, Time-lapse, three-dimensional in situ imaging of ice crystal growth in a colloidal silica suspension, Acta Mater. 61 (2013) 2077–2086.
[100] H. Nishihara , S. Mukai, D. Yamashita, H. Tamon, Ordered macroporous silica by ice templating, Chem. Mater. 17 (2005) 683–689.
[101] L. Qian, A. Ahmed, L. Glennon-Alty, Y. Yang, P. Murray, H. Zhang, Patterned substrates fabricated by a controlled freezing approach and biocompatibility evaluation by stem cells, Mater. Sci. Eng. C Mater. Biol. Appl. 49 (2015) 390–399.
[102] L. Fabietti, R. Trivedi, Development of interface morphologies in the tert butyl alcohol-water system, J. Cryst. Growth 182 (1997) 185–197.